
The Velocity and Timing of Multiple Spherically Converging Shock Waves in Liquid Deuterium

Inertial confinement fusion (ICF) target designs use a sequence of shocks to compress the shell and fuel assembly before they implode.¹ The fuel entropy can be controlled by optimizing the strength and timing of these shocks, thereby minimizing the required driver energy. The goal is to maintain the internal pressure of the fuel to ~ 1 to 2 times its Fermi-degenerate pressure. To achieve these optimal conditions, the four shocks must merge in a precise sequence at the inner surface of the fuel layer.^{2,3} The National Ignition Campaign⁴ for ICF ignition at the National Ignition Facility (NIF)⁵ includes tuning experiments to verify shock timing as a method to set the laser to optimal drive conditions for hohlraum-driven ignition targets.³ Similarly, the fusion program at LLE requires validation of the hydrodynamic codes used in direct-drive ICF implosions. In this article, we report on results of direct-drive experiments that mimic and exceed the conditions for the first three shocks in an ignition target. These experiments develop a shock-timing technique for ignition targets and validate simulations of direct-drive ICF targets.⁶ The development was successful and this technique was applied to full-scale experiments to tune hohlraum-driven ignition targets on the NIF.⁷ To model these experiments, the simulations incorporated a nonlocal model⁶ to treat heat conduction in the coronal plasma. These simulations model shock velocity and timing quite well, providing confidence in the hydrodynamic codes used to design direct-drive ICF targets for OMEGA and the NIF.

In direct-drive ICF, the initial shocks are produced by short (~ 100 -ps) laser pulses preceding the main pulse that drives the implosion.⁸ Short individual pulses are desirable for direct-drive ICF because they are impulsive on hydrodynamic time scales. As a result, only the energy contained in the pulse matters, not the temporal shape. The simple temporal Gaussian pulses that high-power lasers readily produce are ideal for this purpose. Moreover, individual laser pulses provide discrete drive events that can be easily tuned to optimize shock-wave timing. The strength of those shocks depends on the energy in the pulses and on the details of the laser-target-coupling mechanisms. The strength (velocity) of those shocks is a very good measure of the efficiency of that coupling and, therefore,

a sound metric for validating the hydrodynamic codes used to design ICF targets.

These experiments measured the velocity and timing of multiple converging shock waves *inside* spherical targets filled with liquid (cryogenic) deuterium. The drive laser produced a sequence of up to four shocks, whose strength and timing were designed so that later stronger shocks overtake earlier weaker ones to produce multiply shocked deuterium. These shocks ultimately coalesce about $200\ \mu\text{m}$ into the deuterium, forming a single strong shock that converges toward the center of the targets. The shock velocities and the times of these mergers are measured with high precision using time-resolved velocity interferometry⁹ and streaked optical pyrometry.¹⁰ Shock velocity and timing are measured to better than the $\sim 1\%$ and ± 50 -ps precision required for ignition targets. This technique was used on full-scale NIF experiments to tune hohlraum-driven ignition targets.

The OMEGA results are best simulated when the hydrodynamic code uses a nonlocal model⁶ to transport the absorbed laser energy from the coronal plasma to the ablation surface. The simulations replicate the measured shock velocities and shock merger times with high fidelity.

These experiments are the first to time multiple, spherically converging shock waves in liquid deuterium. They produced the highest-reported shock velocities in liquid deuterium and the first observation of an increase in shock strength (velocity) caused by spherical convergence.

These experiments were performed on OMEGA—a 60-beam, 351-nm laser designed to directly drive spherical-target implosions with high-irradiation uniformity.¹¹ The velocity interferometry system for any reflector (VISAR)⁹ detects the Doppler shift of an optical (532-nm) probe beam that reflects off the shock front. To provide diagnostic access to the shock waves, spherical targets were fitted with a diagnostic cone similar to that used in the fast-ignition concept.¹² The targets are described in Ref. 7 and are shown in Fig. 125.1.

The spherical shell and cone were filled with liquid deuterium; VISAR observed the shocks on the inside of the shell through an aperture in the end of the cone.

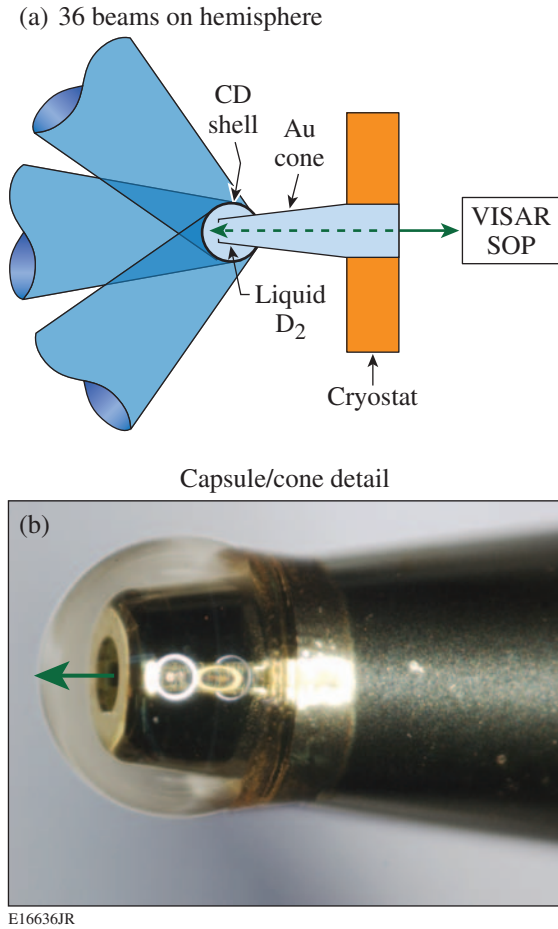


Figure 125.1
 (a) Schematic of target and beam irradiation showing the 900- μm -diam CD sphere with a re-entrant cone [Fig. 125.1(b)], which is irradiated with 36 OMEGA beams. The target and cone are filled with cryogenic liquid deuterium.

The sphere was irradiated by 36 OMEGA beams on its hemisphere opposite the line of sight of VISAR. The beams were fitted with the same SG4-distributed phase plates¹³ used for the 60-beam ICF implosion experiments. Two-dimensional simulations of the irradiation uniformity indicate that this configuration produces a uniform intensity distribution pattern that replicates the 60-beam irradiation uniformity in a region of $\sim\pm 20^\circ$ about the VISAR axis. (VISAR has an $f/3$ collection lens.) These experiments, therefore, produce an accurate surrogate for the shock-transit portion of a spherically symmetric ICF implosion. The liquid deuterium is surrogate for the deuterium–tritium ice layer in an ICF target; it provides an extended, uniform medium for the shocks to propagate. In

addition to VISAR, a streaked optical pyrometer (SOP)¹⁰ was used to observe the optical self-emission from the shocks in the deuterium.

Figure 125.2(a) shows VISAR data for a three-shock experiment (shot 59533) driven by three 100-ps laser pulses (at 0, 1, and 2 ns), which are depicted in the graph overlay in Fig. 125.2(a). The VISAR record is a 1-D image (vertical axis) of the target that is streaked in time (horizontal axis). Imposed on that image is a series of fringes whose vertical position (fringe phase) is proportional to the shock velocity. The image in Fig. 125.2(a) is a view of the shocks in the liquid deuterium

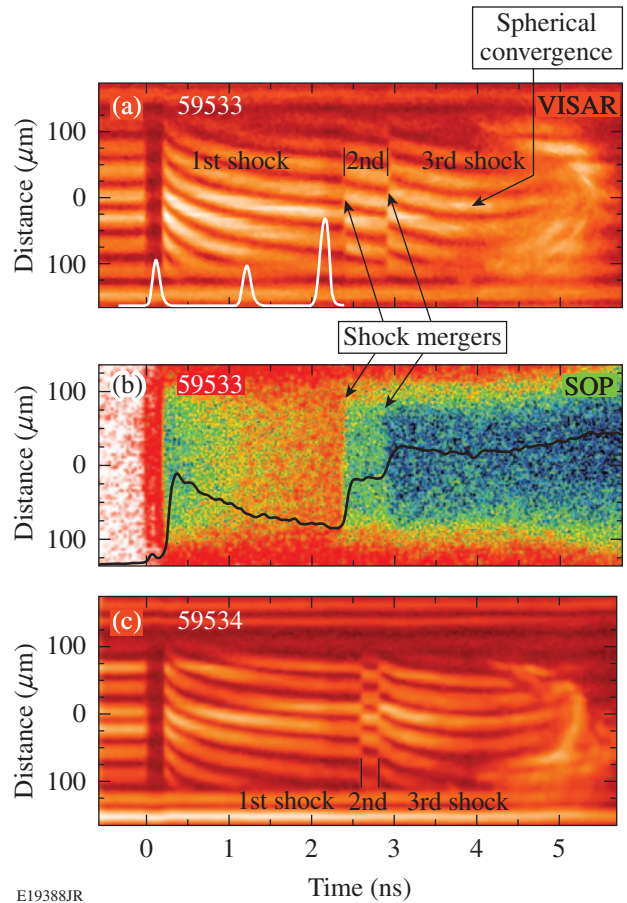


Figure 125.2
 (a) VISAR data record (space versus time) with fringes that represent the velocity of the shocks produced by the laser pulse shown in the figure. The three shocks are observed as well as the jump in fringe position that occurs when the second and third shocks merge at 2.4 and 2.9 ns, respectively. (b) Streaked optical pyrometer (SOP) data showing the self-emission intensity (lineout in figure) follows the shock velocity and shock mergers, providing corroboration of shock timing. (c) VISAR data for shot with lower second pulse and higher third pulse; these delay the first merger and advance the second, illustrating the technique to time shock in a tight sequence.

contained in the shell as observed through the aperture in the re-entrant cone. The experiment was arranged so these shock waves spherically converged along the VISAR axis. VISAR was able to track this convergence until the shock impacted the front of the cone, which was $200\ \mu\text{m}$ from the inside of the sphere.

Before $T = 0$, the fringes in Fig. 125.2(a) are horizontal because there was no shock or movement in the target. At $T = 0$ the signal disappears because the VISAR probe was absorbed by the $10\text{-}\mu\text{m}$ CD shell, which was photoionized by x rays from the laser-produced plasma. After the shock transited the CD and reached the deuterium (which remains transparent), the VISAR signal returns and the fringes abruptly shift in response to the shock velocity in the deuterium. At that time, the shock produced by the short pulse is unsupported and decelerating; the resulting VISAR fringes, therefore, exhibit curvature in time.

At $2.4\ \text{ns}$, the shock produced by the second laser pulse (at $\sim 1\ \text{ns}$) overtakes the first shock. [VISAR did not detect the second shock until it overtook the first because the first shock was reflective (and opaque).] At that point, the coalesced shock (first and second shocks) was stronger and had a higher velocity; VISAR detected this sudden increase in velocity as a jump in fringe position. This is a shock-timing measurement. Since this shock was also unsupported, it decelerated as it traveled through the deuterium and the fringes are seen to slope downward. (The decay rate of this second shock is different than that of the first because the rarefaction wave that produces it now encounters double-shocked deuterium.) At $2.9\ \text{ns}$, the shock from the third pulse (at $2\ \text{ns}$) overtakes that coalesced shock and another jump in velocity occurs. This final shock is also unsupported and begins to decay, producing a downward motion of the fringes in time. At about $4\ \text{ns}$, the fringes curve upward, indicating acceleration. This increase in velocity is a result of spherical convergence. As this final shock (three coalesced shocks) spherically converges, its specific volume decreases and the shock strength increases, producing higher velocities. Lastly, at $\sim 5\ \text{ns}$, the shock impinges on the face of the cone, producing a disturbance that propagates into the cone aperture and the VISAR line of sight. This produced the brighter signal at $5\ \text{ns}$ that moves toward the center of the image as it fills the aperture at $\sim 5.5\ \text{ns}$.

Figure 125.2(b) shows the SOP data acquired simultaneously with the VISAR data in Fig. 125.2(a). This is a color-scaled image (vertical axis) of the self-emission intensity streaked in time (horizontal axis). The solid black line through the image is a plot of the intensity (horizontal lineout) that represents the

temporal profile of shock brightness (temperature), which is proportional to velocity. Note that in response to the various shocks, the SOP intensity decays and jumps in a fashion similar to the VISAR data. SOP provides an independent measure of shock strength and timing.

Figure 125.2(c) shows a VISAR image of a similar experiment (shot 59534) with a slightly modified drive pulse. The second shock was a bit weaker and the third stronger. Compared to Fig. 125.2(a), the first merger in these data occurs later (at $2.6\ \text{ns}$) and the second earlier (at $2.8\ \text{ns}$); this demonstrates a technique to produce a tight sequence of shock arrivals for an ICF target design.

On the NIF, shocks must merge in a tight sequence with a precision of $\pm 50\ \text{ps}$. In the VISAR data, the shock mergers cause a fringe jump that occurs over, at most, two of the 10.6-ps pixels (i.e., $\sim 22\ \text{ps}$). Calibration techniques and the temporal optical fiducials on these data allow one to calibrate the streak cameras to better than 1% precision. Together, they provide the necessary precision to time shock waves on OMEGA and the NIF to the $\pm 50\ \text{ps}$ required for ignition targets.

For direct-drive ICF target designs, radiation–hydrodynamic codes have long used a heuristic *flux-limiter* model to simulate the reduced flux of energy from the corona, where laser energy is deposited, to the ablation surface where pressure is applied to the target. To simulate many experimental results, the heat flux in some regions had to be limited to $\sim 6\%$ of that predicted by the Spitzer–Härm free-streaming limit. Recent direct-drive experiments with laser intensities $\geq 3 \times 10^{14}\ \text{W/cm}^2$ were not well modeled using that flux limiter.^{14,15} We find this is also true for the shock-velocity measurements.

Figure 125.3 shows the velocity profiles measured by VISAR (solid) recorded from a two-shock experiment where the two drive pulses had irradiation intensities of $3 \times 10^{14}\ \text{W/cm}^2$ on a CD sphere filled with deuterium. The dotted curve in Fig. 125.3 shows the shock-velocity profile predicted by LILAC¹⁶ using the flux-limiter model with $f = 0.06$. This flux-limiter value was previously constrained by simulations of various experimental observables. Note in Fig. 125.3 that it underestimates the strength of the first shock. This type of disagreement was also true for recent absorption, acceleration, and scattered-light measurements on OMEGA.¹⁷ The dashed curve in Fig. 125.3 shows the velocities predicted when a nonlocal transport model is used.⁶ This model better simulates the shock velocity produced by the first pulse and the merger time of the two shocks. Early in time, when the first pulse interacts with the solid target,

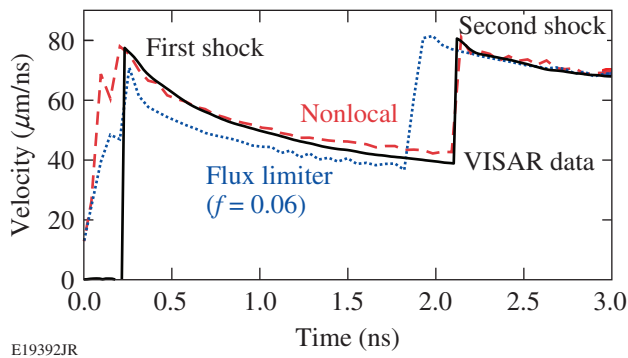


Figure 125.3

The shock-velocity profile (solid) for a two-shock experiment. The profile predicted by *LILAC* using the flux-limiter model with $f=0.06$ (dotted) and using a nonlocal transport model (dashed). The latter better simulates the experiments, particularly the initial interaction with the target and the first shock.

the density scale is very short near the critical density, where the majority of laser light is absorbed. In the flux-limiter model, the classical Spitzer flux is replaced with 6% of the free-stream limit in a narrow region near this surface, where this limit is applied. This produces a nonphysical jump in the electron density near the critical surface, which leads to reduced absorption of laser light. The nonlocal treatment eliminates this jump, resulting in higher laser coupling and a stronger first shock, in better agreement with experimental data. Figure 125.3 shows that proper treatment of this electron transport is essential to correctly model these plasmas and predict shock timing.

Figure 125.4 shows the measured (solid)-velocity profile from an experiment (shot 59667) that used a 900- μm -diam, 5- μm -thick CH shell filled with liquid deuterium. The triple-pulse drive is shown in the figure. The dotted curve in Fig. 125.4 is the simulated velocity that matches the experiment to better than the ± 50 ps required for ignition targets. Also shown is a lineout (dashed) of the SOP self-emission intensity versus time; it also provides a corroborative measure of shock velocities and shock mergers. These data also show the acceleration caused by convergence effects, as predicted by the simulations. In 5- μm -shell targets, the laser fully ablates the CH shell and begins to interact with the deuterium. The ability to model this phase is critical to the performance of direct-drive-ignition targets, which are expected to have very thin CH shells.

That the simulations accurately predict the first shock velocity indicates that the codes adequately treat the plasma-initiation problem. Similarly, the good agreement with the subsequent shock velocities indicates the expansion of the coronal plasma, and the interaction of later pulses with that preformed plasma is also well modeled. Lastly, the agreement

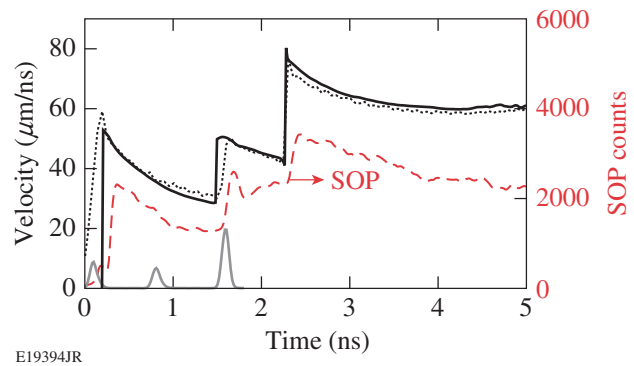


Figure 125.4

Measured-velocity profile (solid) and self-emission intensity (dashed) for a three-shock experiment. The simulated-velocity profiles (dotted) predict the velocities of each shock and their merger times with good accuracy including the effect of convergence.

of the predicted velocities and merger times with experiments indicates that the material properties (equations of state for CH and deuterium) used in the codes are also adequate. Obtaining good simulation of these data depended greatly on locating the target to within ~ 30 μm of the desired position. This ensured that the irradiation uniformity and intensity were as designed and expected.

A direct-drive ICF implosion on OMEGA has a longer (~ 1 -ns) fourth pulse that drives the target implosion. This pulse is more intense and has significantly higher energy than the individual ~ 100 -ps pulses preceding it. For shock-timing experiments, x rays from that drive pulse can be sufficiently intense to photoionize the quartz window at the end of the VISAR cone; this could prevent VISAR measurements. Figure 125.5 shows the VISAR signal from a four-pulse experiment where a reduction in the drive-pulse intensity made it possible to measure all four shocks using VISAR. The features of the data are similar to those in Figs. 125.2(a) and 125.2(c): the merger of the second shock with the first is evident at 1.9 ns; then at 2.4 ns the third shock merges with the first two. At 3.1 ns, the fourth shock from the main drive pulse (which started at 2 ns) overtakes the three merged shocks; soon after, the VISAR signal disappears. It is likely that, at these high pressures, the shock was sufficiently hot to photoionize the unshocked deuterium ahead of it and this material absorbed the VISAR probe beam.

In Fig. 125.6, the solid line is the velocity profile deduced from the VISAR data, showing shock velocities of 50, 56, 73, and 130 km/s for each of the four shocks. The latter velocity corresponds to a pressure of 2500 GPa in the deuterium. Ignition targets on the NIF will have the first three shock velocities in the range of 20, 40, and 70 km/s. These results

show that spherical shocks of those strengths in deuterium can readily be observed and timed using this technique. Note in Fig. 125.6 that the SOP (dashed) signal decreases (but does not disappear) at ~ 2.4 ns. This could be the result of initial blanking of the quartz window; the main pulse reaches its peak at this time. SOP detects light in the 590- to 850-nm range; photons in this range are better absorbed than those of the VISAR probe.

The velocity and timing of multiple, spherically converging shock waves have been measured in cryogenic-deuterium targets directly irradiated with laser pulses. A shock velocity of 135-km/s was observed in cryogenic deuterium. This is the highest shock velocity ever reported in deuterium and corresponds to a pressure of ~ 2500 GPa (25 Mb). This is also the first measurement of shock velocities that exhibited the effects

of spherical convergence, i.e., the increase in shock strength produced by that convergence.

To properly simulate these results, the hydrodynamic code used a nonlocal model to properly simulate heat transport in the coronal plasma. At high intensities, the initial plasmas produced by short (100-ps) pulses have steep density and temperature gradients, which the standard flux-limiter models do not properly treat. When a nonlocal thermal transport model is used instead, the shock velocities and timing are better modeled by the simulations. The ability to simulate these experimental results provides confidence in the hydrodynamic codes used to design direct-drive ICF targets for OMEGA and the NIF.

These experiments are the first to time multiple, spherically converging shock waves in liquid deuterium. The observed deuterium shock velocities were similar to and greater than those required for the initial phase of an ignition target on the NIF. They demonstrate the ability to time and control shock waves to the precision needed for ignition experiments. This technique was applied to full-scale experiments to tune hohlraum-driven ignition targets on the NIF.

ACKNOWLEDGMENT

This work was supported by the U.S. Department of Energy Office of Inertial Confinement Fusion under Cooperative Agreement No. DE-FC52-08NA28302, the University of Rochester, and the New York State Energy Research and Development Authority. The support of DOE does not constitute an endorsement by DOE of the views expressed in this article.

REFERENCES

1. J. D. Lindl, *Inertial Confinement Fusion: The Quest for Ignition and Energy Gain Using Indirect Drive* (Springer-Verlag, New York, 1998), Chap. 6, pp. 61–82.
2. D. H. Munro *et al.*, Phys. Plasmas **8**, 2245 (2001).
3. D. H. Munro, H. F. Robey, B. K. Spears, and T. R. Boehly, Bull. Am. Phys. Soc. **51**, 105 (2006).
4. B. A. Hammel and the National Ignition Campaign Team, Plasma Phys. Control. Fusion **48**, B497 (2006).
5. E. I. Moses, Fusion Sci. Technol. **54**, 361 (2008).
6. V. N. Goncharov, T. C. Sangster, P. B. Radha, R. Betti, T. R. Boehly, T. J. B. Collins, R. S. Craxton, J. A. Delettrez, R. Epstein, V. Yu. Glebov, S. X. Hu, I. V. Igumenshchev, J. P. Knauer, S. J. Loucks, J. A. Marozas, F. J. Marshall, R. L. McCrory, P. W. McKenty, D. D. Meyerhofer, S. P. Regan, W. Seka, S. Skupsky, V. A. Smalyuk, J. M. Soures, C. Stoeckl, D. Shvarts, J. A. Frenje, R. D. Petrasso, C. K. Li, F. Séguin, W. Manheimer, and D. G. Colombant, Phys. Plasmas **15**, 056310 (2008).

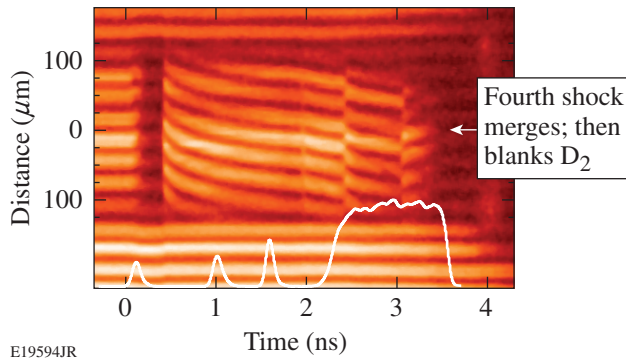


Figure 125.5
VISAR image for a four-shock experiment using an ICF drive pulse shown in the figure. Three shocks are visible as in Fig. 125.2(a) with mergers at 1.6 and 2.3 ns. At 3.1 ns, the fourth shock (produced by the main pulse) overtakes them, and soon after the x-ray flux from that pulse blanks the VISAR window.

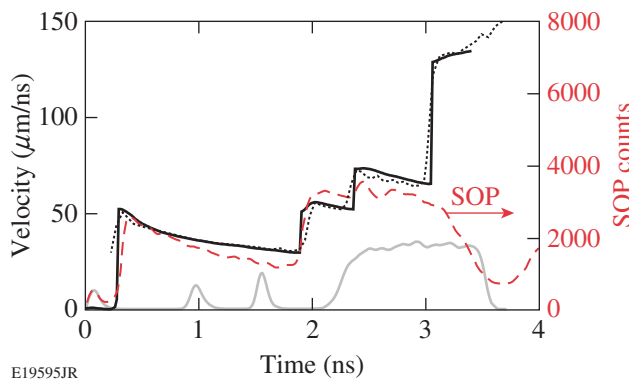


Figure 125.6
The velocity profile (solid) showing velocities of 42, 64, 83, and 135 km/s for each of the four shocks and the simulation (dotted). The latter velocity corresponds to a pressure of 2500 GPa. The SOP signal (dashed) follows VISAR during the first three shocks but then decreases at ~ 2.4 ns. Laser pulses are shown at the bottom of the graph.

7. T. R. Boehly, D. H. Munro, P. M. Celliers, R. E. Olson, D. G. Hicks, V. N. Goncharov, G. W. Collins, H. F. Robey, S. X. Hu, J. A. Marozas, T. C. Sangster, O. L. Landen, and D. D. Meyerhofer, *Phys. Plasmas* **16**, 056302 (2009).
8. V. N. Goncharov, in *Laser-Plasma Interactions*, edited by D. A. Jaroszynski, R. Bingham, and R. A. Cairns, Scottish Graduate Series (CRC Press, Boca Raton, FL, 2009), pp. 409–418.
9. P. M. Celliers, D. K. Bradley, G. W. Collins, D. G. Hicks, T. R. Boehly, and W. J. Armstrong, *Rev. Sci. Instrum.* **75**, 4916 (2004).
10. J. E. Miller, T. R. Boehly, A. Melchior, D. D. Meyerhofer, P. M. Celliers, J. H. Eggert, D. G. Hicks, C. M. Sorce, J. A. Oertel, and P. M. Emmel, *Rev. Sci. Instrum.* **78**, 034903 (2007).
11. T. R. Boehly, D. L. Brown, R. S. Craxton, R. L. Keck, J. P. Knauer, J. H. Kelly, T. J. Kessler, S. A. Kumpan, S. J. Loucks, S. A. Letzring, F. J. Marshall, R. L. McCrory, S. F. B. Morse, W. Seka, J. M. Soures, and C. P. Verdon, *Opt. Commun.* **133**, 495 (1997).
12. R. Kodama *et al.*, *Nature* **412**, 798 (2001).
13. Y. Lin, T. J. Kessler, and G. N. Lawrence, *Opt. Lett.* **20**, 764 (1995).
14. W. Seka, V. N. Goncharov, J. A. Delettrez, D. H. Edgell, I. V. Igumenshchev, R. W. Short, A. V. Maximov, J. Myatt, and R. S. Craxton, *Bull. Am. Phys. Soc.* **51**, 340 (2006).
15. W. Seka, D. H. Edgell, J. F. Myatt, A. V. Maximov, R. W. Short, V. N. Goncharov, and H. A. Baldis, *Phys. Plasmas* **16**, 052701 (2009).
16. J. Delettrez, R. Epstein, M. C. Richardson, P. A. Jaanimagi, and B. L. Henke, *Phys. Rev. A* **36**, 3926 (1987).
17. W. Seka, D. H. Edgell, J. P. Knauer, J. F. Myatt, A. V. Maximov, R. W. Short, T. C. Sangster, C. Stoeckl, R. E. Bahr, R. S. Craxton, J. A. Delettrez, V. N. Goncharov, I. V. Igumenshchev, and D. Shvarts, *Phys. Plasmas* **15**, 056312 (2008).